Please cite the Published Version

Additional Information: This is an Author Accepted Manuscript of an article published in Applied Surface Science.

Magnetron co-sputtered $Bi_{12}TiO_{20}$/$Bi_4Ti_3O_{12}$ composite – an efficient photocatalytic material with photoinduced oxygen vacancies for water treatment application

Matthieu Grao[1], Marina Ratova[1*], James Redfern[2], Peter J Kelly[1]

[1] Surface Engineering Group, Department of Engineering, Manchester Metropolitan University, Manchester, M1 5GD, UK

[2] Department of Natural Sciences, Manchester Metropolitan University, Manchester, M1 5GD, UK

[*] Corresponding author: Dr Marina Ratova, Department of Engineering, Manchester Metropolitan University, John Dalton Building, Chester Street, Manchester M1 5GD, UK, email: marina_ratova@hotmail.com; Tel.: +44-161-247-4648

Abstract

$Bi_{12}TiO_{20}$/$Bi_4Ti_3O_{12}$ composite photocatalyst was investigated as an alternative to the conventionally used titanium dioxide, to tackle the well-known drawbacks of fast charge-carriers recombination and low quantum efficiency of TiO_2. Polycrystalline $Bi_{12}TiO_{20}$/$Bi_4Ti_3O_{12}$ thin films were produced by pulsed DC reactive magnetron co-sputtering, a method of high industrial relevance, and compared to titanium dioxide coatings produced with the same technique. Following the deposition process, optimum thermal treatment temperature and length were established, to obtain crystallisation. The synthesised coatings were thoroughly analysed with a range of techniques, including Raman spectroscopy, XRD, SEM, TEM, EDX, XPS and AFM. The photocatalytic properties of $Bi_{12}TiO_{20}$/$Bi_4Ti_3O_{12}$ composite were assessed through methylene blue degradation and *E. coli* inactivation tests under UV-A irradiation. The results indicated considerably higher efficiency of the composite photocatalyst when compared to TiO_2. Moreover, the reusability assessment of $Bi_{12}TiO_{20}$/$Bi_4Ti_3O_{12}$ thin films revealed an incremental performance increase after each consecutive test, leading to a 6-fold increase in photocatalytic activity between the first and 15th cycle. Time-

resolved photoluminescence and XPS analysis highlighted an increased presence of oxygen vacancies, forming over repeated usage of bismuth titanate, leading to longer lifetimes of photogenerated species and enhanced photocatalytic performance.

Keywords: Bismuth titanate; Photocatalyst; Magnetron sputtering; Water treatment; Titanium dioxide.

1. **Introduction**

According to the World Health Organization, over two billion people worldwide still lack access to safely-managed water [1]. Untreated water is likely to harbour pathogenic microorganisms that can cause life-threatening diseases such as cholera, dysentery, typhoid, polio and diarrhoea [1]. Furthermore, it is predicted that half of the world's population will live in water stressed areas by 2025. As a result, access to adequate provision of water resources is considered a global priority and is named as one of the UN Sustainable Development Goals [2]. This pressing issue calls for novel sustainable and inexpensive technologies to be developed and implemented, to rise up to the challenge.

Photocatalysis is an advanced oxidation process (AOP), which has shown great potential for wastewater treatment. It is an efficient, economical and sustainable process, as it only requires a photocatalyst, a light source and treated media to operate. When exposed to photons of higher energy than its bandgap ($hv \geq Eg$), a photocatalyst is able to generate charge carriers: electron-hole pairs. These charge carries diffuse to the surface of photocatalyst, react with water and oxygen to form reactive oxygen species (ROS), such as $OH^{\bullet}$ and $O_2^{\bullet-}$, capable of mineralising toxic organic compounds [3]. Additionally, photogenerated ROS have demonstrated antimicrobial properties [4], with the potential to limit other microbial processes that lead to increased virulence [5].

To date, crystalline titanium dioxide remains the most widely studied and used photocatalyst whose properties were discovered by Fujishima and Honda in 1969 [6]. The most photocatalytically active

polymorph, anatase, is a wide bandgap semiconductor with a bandgap energy of 3.2 eV. It is known for its ability to mineralise a wide range of organic compounds when exposed to UV light [7]. Unfortunately, UV accounts for less than 5% of the solar spectrum, which limits its potential for outdoor solar applications. Moreover, it suffers from a rapid electron-hole recombination [3]. Combination of these two factors makes practical exploitation of titanium dioxide photocatalysis a rather challenging task for real-world high-throughput processes. Various attempts have been made to address these issues by either modifying TiO_2 [8], [9] or using alternative photocatalysts [10]–[12]. Lately, bismuth oxide-based materials have captured researchers' attentions, as possible viable alternatives to titanium dioxide. Bismuth oxide [13], vanadate [14], tungstate [15] and titanate [16] consistently displayed high photocatalytic activity and lower band gap, compared to conventionally used titania. Despite initially promising results, the overall number of studies of bismuth (complex) oxide-based materials is rather limited.

Bismuth titanate (BT) is a complex oxide semiconductor characterised by a high curie temperature, high dielectric constant and low dielectric energy loss. Hence, this ferroelectric material is mainly used as a replacement for lead-based ceramics in capacitors, sensors and actuators [16]. However, in recent years, it was also investigated for its photocatalytic properties; with two polymorphs namely, $Bi_{12}TiO_{20}$ and $Bi_4Ti_3O_{12}$, having shown promising results [17], [18]. The former belongs to the Sillenite family and is formed by a network of Bi–O polyhedron connected to TiO_4 tetrahedron [19]. The latter belongs to the Aurivillius family and is composed of pseudo-perovskite units $(Bi_2Ti_3O_{10})^{2-}$, sandwiched by fluorite-like $(Bi_2O_2)^{2+}$ layers [20].

In 2003, Yao *et al.* was the first to report the remarkable photocatalytic activity of $Bi_{12}TiO_{20}$, which is believed to be the most active of the two studied polymorphs [17]. The Bi–O polyhedra are suggested to act as active donor sites, which can enhance O_2 electron transfer and reduce electron-hole pairs recombination. $Bi_{12}TiO_{20}$ has a low bandgap, estimated at 2.4 eV, and therefore can be photoactivated with a broader range of wavelengths, compared to titanium dioxide.

Recent studies are focused on producing a new generation of bismuth titanate-based composites, to improve light harvesting and extend charge carrier lifetime. Du *et al*. synthesized an efficient $Bi_{12}TiO_{20}/Bi_4Ti_3O_{12}$ photocatalyst composite using low-energy solid-state reaction [21]. Single phase samples were all outperformed by mixed phases ones, with the highest activity being achieved for a Bi:Ti molar ratio of 12:6. Similarly, Meng *et al*. synthesized porous $Bi_{12}TiO_{20}/Bi_4Ti_3O_{12}$ composite nanofibers using electrospinning [22]. The best performing sample had a $Bi_{12}TiO_{20}:Bi_4Ti_3O_{12}$ molar ratio of 11.5:1 and showed excellent photocatalytic activity, cycling stability, and regeneration ability. Photogenerated electrons with low reduction potential in the $Bi_{12}TiO_{20}$ conduction band migrate to the $Bi_4Ti_3O_{12}$ valence band to recombine with low oxidation potential holes [21]. Consequently, electron and holes with high redox potential are less likely to recombine and more likely to diffuse to the surface.

It should be noted that, to date, photocatalytic bismuth titanate photocatalysts were synthesised mainly via soft chemistry routes [23], [24] and solid-state reaction [18], potentially limiting their commercial exploitation. In contrast to chemical techniques, physical vapour deposition methods such as magnetron sputtering technique offer multiple advantages, such as lack of toxic / hazardous precursors and intermediates, precise control over material uniformity and composition and great up-scaling potential.

Bismuth titanate coatings were prepared by reactive pulsed DC (pDC) magnetron co-sputtering onto soda-lime glass slides. This technique has the advantage of direct immobilisation of the catalyst which provides the added advantage of easy material recovery from treated media, unlike powdered photocatalysts, where membrane filtration is typically required, contributing to the overall cost of the treatment process [25]. Additionally, magnetron sputter deposition provides a high level of control over chemical and morphological properties [25]. Several studies have reported bismuth titanate production via magnetron sputter deposition [26]–[28], however these studies are based on the use of compound targets. In contrast to that, sputtering of metallic targets in a reactive oxygen

containing atmosphere allows deposition at considerably lower cost (no sophisticated radio-frequency power sources required); enables higher deposition rates and therefore shorter deposition times; and is less prone to arcing / process failures. This work presents the deposition of photocatalytic bismuth titanate films via pDC reactive magnetron co-sputtering; to the best of our knowledge, this technique has not been reported for the production of bismuth titanate to date. Following the deposition process, the produced materials were thoroughly characterised by a variety of analytical techniques and the photocatalytic properties were studied via dye degradation and *E. coli* inactivation tests. Conventionally used photocatalytic titanium dioxide films were deposited using the same technique and compared to bismuth titanate. The results of the study confirmed the high efficiency of bismuth titanate compared to its titanium dioxide counterpart.

2. Experimental

2.1. Deposition process

BT thin films were deposited using a Nordiko sputtering rig (schematic given in supplementary material (S1)), described in detail in an earlier work [29]. In brief, deposition was performed from metallic bismuth (300 mm × 100 mm, 99.5% purity, bonded to a copper backing plate) and titanium (300 mm × 100 mm, 99.5% purity, directly cooled) targets fitted onto two Teer Coatings Ltd unbalanced type II magnetrons. The magnetrons were powered by an Advanced Energy Pinnacle Plus dual channel power supply in pulsed DC mode operating at a frequency of 100kHz and 60% duty. The sputtering process was carried out in reactive mode, in an argon / oxygen atmosphere (50 and 25 sccm flow of argon and oxygen, respectively), with MFCs controlled by a Speedflo controller from Gencoa, to a partial pressure of 0.44 Pa. The thin films were deposited onto soda-lime glass slides ultrasonically pre-cleaned in acetone (Sigma Aldrich).

2.2. Characterisation

Raman spectroscopy and Raman mapping were performed with a DXR Raman microscope from Thermo Scientific. The laser was operated at a wavelength of 532 nm, with a power of 10 mW, 900 lines per mm grating, a long working distance microscope objective with magnification of 50, an estimated spot size of 1.1 μm and a 25 μm pinhole. 1677 Raman spectra were acquired using a step size of 100 μm along the Y and X axes. The thin film crystallographic information was obtained with X-ray diffraction (XRD), on a Panalytical Xpert system. CuKα1 radiation at 0.154 nm was used, in grazing incidence mode at 3°, over a scan range from 20 to 70° 2θ; the accelerating voltage and applied current were set to 40 kV and 30 mA respectively. The coatings morphology was analysed with scanning electron microscopy (SEM) using a Zeiss Supra 40 VP-FEG-SEM. Further analysis of surface morphology and surface roughness data were obtained using a Horiba XPlora Plus atomic force microscopy (AFM) system. The HRTEM micrographs were obtained using a FEI Titan Themis FEG STEM equipped with a super-X energy-dispersive X-ray spectroscopy (EDX) system; prior to that, a FEI Helios G4CX FIB-SEM was used to extract a lamella from the bulk of a $Bi_{12}TiO_{20}/Bi_4Ti_3O_{12}$ sample. The oxidation state information was obtained using X-ray photoelectron spectroscopy (XPS), performed with a SUPRA photoelectron spectrometer (Kratos Analytical Ltd.) equipped with Mg K X-rays as the primary excitation source. The binding energy was referenced to the C 1s line at 284.8 eV for calibration. Curve fitting was performed applying a Gaussian function. The sample's thickness was measured by creating an artificial step, by covering part of the microscope soda-lime slide with Kapton tape prior to the deposition. A Profilm3D interferometer from Filmetrics, with a magnification of x50, was used to measure the height of the artificial step. Time-resolved photoluminescence (PL) analysis was performed externally on selected samples, with Edinburgh Instruments FLS1000 Photoluminescence Spectrometer, using Nd:YAG laser as the excitation source with an excitation wavelength of 355nm. The PL decay profiles were normalised to maximum intensity value (based on material emission spectrum identified with PL mapping): 510 nm for titanium dioxide samples and 540nm for bismuth titanate samples. The PL decay profiles were fitted using Fluoracle software package.

2.3. Dye degradation test

Samples of 2 cm ×2.5 cm was cut and immersed in a 50 mL solution of methylene blue (Alfa Aesar) with a concentration of 2 µmol/L. The samples were left in the dark for 60 minutes under continuous stirring, at room temperature to reach adsorption-desorption equilibrium. Then they were irradiated by a UV-A lamp (2×15 W Sankyo Denki BLB lamps, peaked at 365 nm) for 60 minutes. The integrated irradiance value in the wavelength range 200–800 nm was measured at 273 W m^{-2}. The main MB absorption peak at 664 nm was monitored with an Ocean Optics USB4000 UV-Visible spectrometer. Plotting the absorbance against the time allows the extraction of the apparent first order rate constant, k, by calculating the slope of the line, as described in earlier work [30]. The calculated k values have been used to compare the photocatalytic efficiency of each sample. All tests were performed in triplicate to obtain mean values of k.

2.4. Maintenance and standardisation of microorganisms and media

Escherichia coli NCTC 9001 was subcultured from stock stored in at -80°C and maintained on tryptone soya agar (TSA) (Oxoid, Basingstoke) at 4 C°. For testing antimicrobial photocatalytic activity, 2-4 colonies of *E. coli* were inoculated into 10 mL of Tryptone Soya broth (TSB, Oxoid, Basingstoke) and grown for 22 ±1 hour at 37 °C with agitation (180 rpm). Cells were harvested by centrifugation (4000 rpm, 10 min) and resuspended in sterile saline water to an optical density of 1.0 at 540 nm (Jenway 6305 Spectrophotometer, UK) resulting in an average "standardised cell suspension" of 1.21x10^8 CFU.mL^{-1}. Neutralizer media was prepared by mixing sodium thiosulphate 3 g/L, Polysorbate 80 30g/L, Lecithin 3 g/L and distilled water up to 1L and sterilized by autoclave for 15 minutes at 121°C.

2.5. Testing for antimicrobial activity

Testing for photocatalytic antimicrobial activity was carried out using a modified version of the BS ISO 27447 [31]. Uncoated glass, BT750 and TiO_2 coated glass coupons (2 cm × 2.5 cm) were

sterilized by autoclaving for 15 minutes at 121°C. Each coupon was inoculated with 10 µl of standardised cell suspension (as described above) and covered with a sterile piece of polypropylene film of the same size. Coupons, in duplicate, were placed in sterile plastic petri plates, which in turn was placed in a larger petri plate containing moistened paper towel to retain humidity. The coupons were placed at a distance of 30 cm from the UVA lamp (15 W Sankyo Denki BLB lamps, peaked at 365 nm). The irradiance received by the coupons, through the petri plates was measured at 0.25 mW cm^{-2}, by a UVP UVX radiometer. To verify the presence of photocatalytic activity, dark control experiments (no irradiation) were performed, following the same experimental protocol but with the petri plates wrapped in aluminium foil. Coupons were incubated under these conditions for the required experimental time (24 or 48 hours), and then were recovered into neutralizer media and serially diluted ten-fold in sterile saline to a dilution on 10^{-7}. 100 µl of each dilution was spread on to Tryptone Soya Agar (TSA), in duplicate and incubated overnight at 37°C. Colonies were counted and the number of colonies forming units (CFU) per mL of the original suspension were calculated. The whole experiment was repeated three times to ensure reproducibility.

3. Results and Discussion

3.1. Deposition

Soda-lime glass slides were coated with bismuth titanium oxide by reactive pulsed DC magnetron sputtering. Bismuth titanium oxide samples were synthesized in an argon/oxygen reactive atmosphere for 4h by rotating the substrates between the two targets, whilst simultaneously sputtering both. Different coating compositions were obtained by varying the power applied to the Ti target from 0.5 to 1.5 kW with 0.25 kW increments, whilst keeping the power applied to the Bi fixed at 0.2 kW. TiO$_2$ samples were also deposited in an argon/oxygen reactive atmosphere, with 1 kW applied to the Ti target, without rotation for 1 hour (conditions were established in an earlier study for production of photocatalytically active titanium dioxide films) [29]. All depositions were operated with a pulse frequency of 100 kHz, a duty cycle of 60 %, while all samples were annealed in

air at 600 °C post-deposition. BT samples were named according to the power applied to the titanium target. All the produced samples are presented in Table 1, with their respective deposition conditions.

Table 1. Coating deposition parameters.

Sample ID	Ti target power	Bi target power	Rotation	Deposition time
	kW	kW	Rpm	h
TiO_2	1	-	-	1
BT500	0.5	0.2	2	4
BT750	0.75	0.2	2	4
BT1000	1	0.2	2	4
BT1250	1.25	0.2	2	4
BT1500	1.5	0.2	2	4

3.2. Characterization

Initially, the bismuth titanate samples were analysed with Raman spectroscopy coupled with Raman mapping for identification of crystalline phases and assessment of their uniformity. According to the literature, $Bi_{12}TiO_{20}$ is the most photocatalytically active phase of bismuth titanate [17]. The results of Raman spectroscopy revealed the presence of $Bi_{12}TiO_{20}$ phase for all the prepared films. However, depending on deposition conditions, the intensity of the Raman peaks for $Bi_{12}TiO_{20}$ and homogeneity of their distribution varied significantly. Of the Raman peaks observed (Figure 1a), peaks identified at 720 and 664 cm^{-1} are due to the stretching of TiO_4 tetrahedrons, whilst the ones at 620, 320, 262, 224 and 206 cm^{-1} are attributed to the vibration modes of the Bi-O [32]. The 166 cm^{-1} peak is attributed to the "breathing mode" of Bi and all O atoms, the 144 cm^{-1} to the "breathing mode" of Bi and O2 atoms, and Bi and O2 to the vibrations elongating the cluster along the [100] or [010] [32]. The most intense Raman peak at 537 cm^{-1} corresponds to the "breathing" of O1 atoms and was used as a reference to produce the Raman maps and assessment of $Bi_{12}TiO_{20}$ phase distribution and uniformity. As can be seen from Raman mapping results (Figure 1 (b, c)), application of lower levels of power to the titanium target resulted in deposition of samples with intense signals and an evenly

distributed $Bi_{12}TiO_{20}$ phase. Increasing the power applied to the titanium target resulted in lower 537 cm^{-1} Raman peak intensities and uneven distributions of the $Bi_{12}TiO_{20}$ phase, with clusters of crystallised $Bi_{12}TiO_{20}$ (red) surrounded by an amorphous structure (green), as shown in Figure 1d. Based on Raman mapping results, the deposition conditions used for the production of sample BT750 were selected for further studies. Additionally, cross-sections of samples TiO_2, BT1500, BT750 and BT500 samples were characterised by EDX analysis and k-factors were estimated using the Schriber-Wims fitting model for elemental quantification (data presented in the Table 2). As expected, increasing the power applied to the Ti target resulted in an increased proportion of titanium within the coatings, which hindered the crystallisation of the $Bi_{12}TiO_{20}$ phase, when the applied power was higher than 750 W.

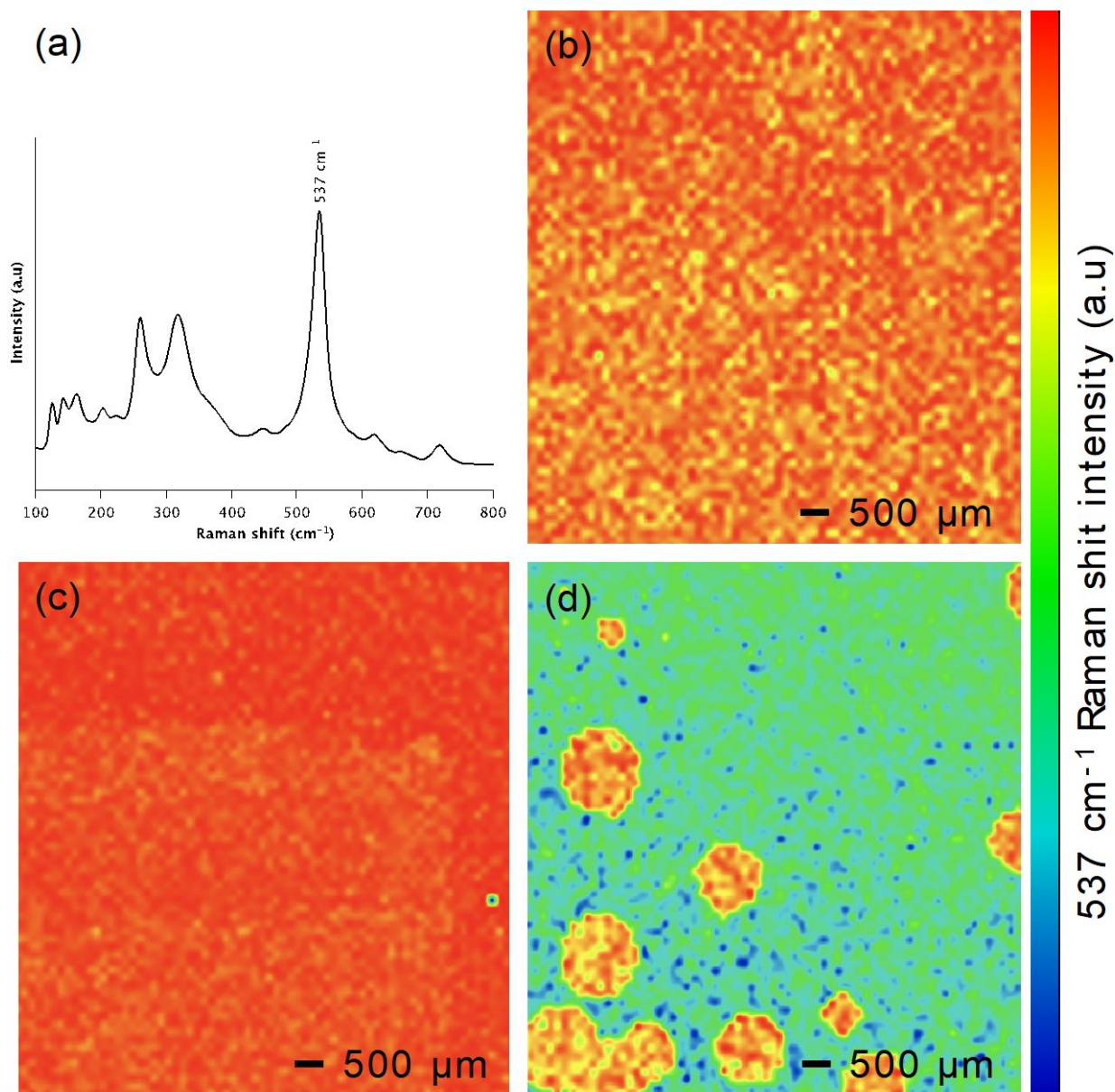*Figure 1. Raman spectrum of (a) $Bi_{12}TiO_{20}$ phase and corresponding Raman mapping of samples (b) BT500, (c) BT750 and (d) BT1500.*

Table 2. Results of elemental analysis (EDX)

Sample	Z	Element	Family	Atomic fraction (%)	Mass fraction (%)	Fit error (%)
TiO$_2$	8.00	O	K	50.90	27.90	0.05
	22.00	Ti	K	49.10	72.10	0.04
	8.00	O	K	35.90	6.57	0.13
BT1500	22.00	Ti	K	23.50	11.50	0.08
	83.00	Bi	L	40.70	81.90	0.04
BT750	8.00	O	K	39.60	6.55	0.96

	22.00	Ti	K	11.80	5.24	0.12
	83.00	Bi	L	48.50	88.20	0.04
	8.00	O	K	37.40	5.79	0.67
BT500	22.00	Ti	K	9.45	3.91	0.09
	83.00	Bi	L	53.10	90.30	0.05

Following phase analysis and mapping, optimum annealing temperatures and times were identified using XRD analysis. The crystallisation and phase transition processes were investigated by placing an as-deposited BT750 sample into an XRD hot stage chamber, for in-situ X-ray diffraction study at varied temperatures. The sample was heated from room temperature to 600 °C with 100 °C increments, in an air atmosphere; detailed phase and crystal plane identification are given in supplementary material (Table S2). As shown in Figure 2, no crystallisation occurs below 400 °C and samples annealed at lower temperatures are characterised by an amorphous structure. The crystallisation starts at 400 °C with formation of the δ-Bi_2O_3 phase (ICDD 96-101-0312), with rather broad diffraction peaks. Annealing at 500 °C results in disappearance of the δ-Bi_2O_3 phase and formation of bismuth titanate polymorphs, identified as $Bi_{12}TiO_{20}$ (ICDD 96-403-0657) and $Bi_4Ti_3O_{12}$ (ICDD 96-152-8446). Finally, at 600 °C, the $Bi_4Ti_3O_{12}$ phase (ICDD 96-152-8446) became more prominent with sharpened diffraction peaks and additional ones appearing. Higher annealing temperatures could not be investigated due to the nature of the substrate used. Therefore, an annealing temperature of 600 °C was identified as the preferential one for achieving BT750 sample crystallisation. Titanium dioxide samples were annealed under identical conditions to enable direct comparison; all observed peaks can be indexed to anatase TiO_2 (ICDD 96-900-8215), as shown in Figure 2a. Additionally, different annealing times (up to 4h) were studied at 600 °C to monitor potential phase transitions depending on annealing duration. The results are presented in Figure 2b and reveal no changes in phase or texture of sample BT750, suggesting that the shortest thermal treatment time of 1h is adequate in this case. Overall, the findings on $Bi_{12}TiO_{20}$/$Bi_4Ti_3O_{12}$ phase transition temperatures were consistent with the results reported in earlier studies on the same

material [16], [24], with annealing time for 1 hour at 600 °C being adequate thermal treatment regime. The annealing temperatures above 600 °C were not considered, due to softening temperatures of soda-lime glass (soda-lime glass reportedly softens at temperatures above 680 °C [33]). Additionally, the crystalline phases were quantified by extracting the weight fractions as percentages from a Pawley intensity refinement, given in supplementary material (S3), based on the areas of two non-overlapping peaks: $Bi_{12}TiO_{20}$ (020) and $Bi_4Ti_3O_{12}$ (600). The estimated phase composition of the BT750 sample is ~80% of the $Bi_{12}TiO_{20}$ phase and ~20% of the $Bi_4Ti_3O_{12}$ phase.
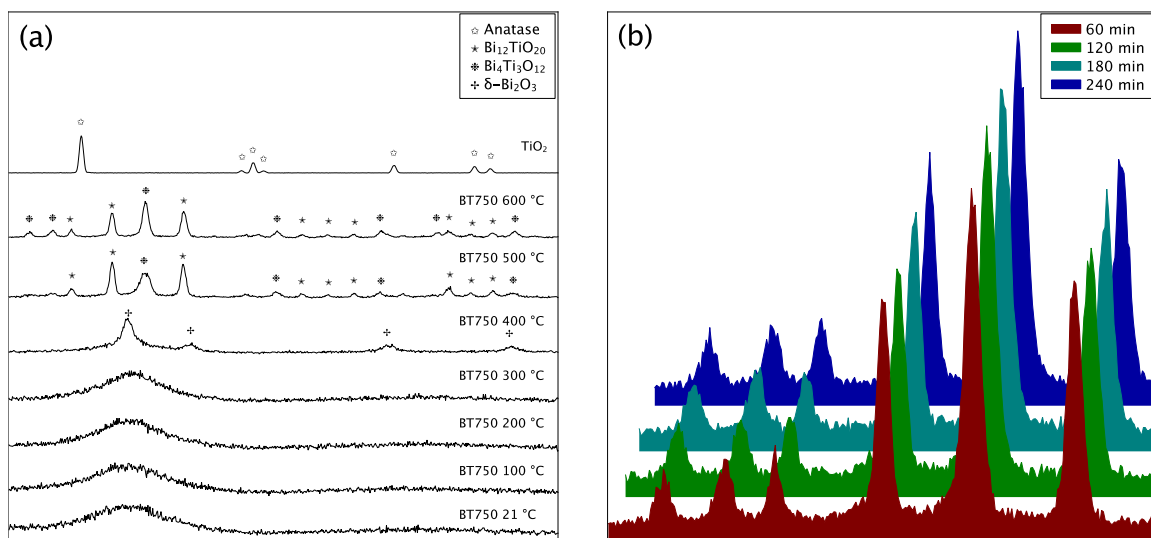

Figure 2. Results of XRD analysis; (a) XRD patterns of sample BT750 heated in an air from room temperature to 600 °C and pattern of TiO_2 annealed at 600 °C; (b) XRD patterns of BT750 sample heated in an air at 600 °C for up to 4 hours.

The surface morphology of the titanium dioxide and bismuth titanate coatings was studied with FEG-SEM; the micrographs are presented in Figure 3 (a, b), respectively. It is clear that there are some morphological differences between these two materials. TiO_2 has a homogeneous cauliflower-like structure, typical for thin film grown by magnetron sputtering [29], while the BT750 sample developed a rather heterogeneous structure, composed of angular crystallites, randomly distributed and embedded in a smooth matrix. Further studies of surface morphology were performed by AFM

(results for TiO$_2$ and BT750 are shown in Figure 3 (c, d), respectively). It should be noted, that despite differences in morphology, similar surface roughness (R$_a$) values of 14.20 nm and 15.56 nm were obtained by AFM for TiO$_2$ and BT750, respectively, thus enabling direct comparison of photocatalytic properties in terms of sample surface area.
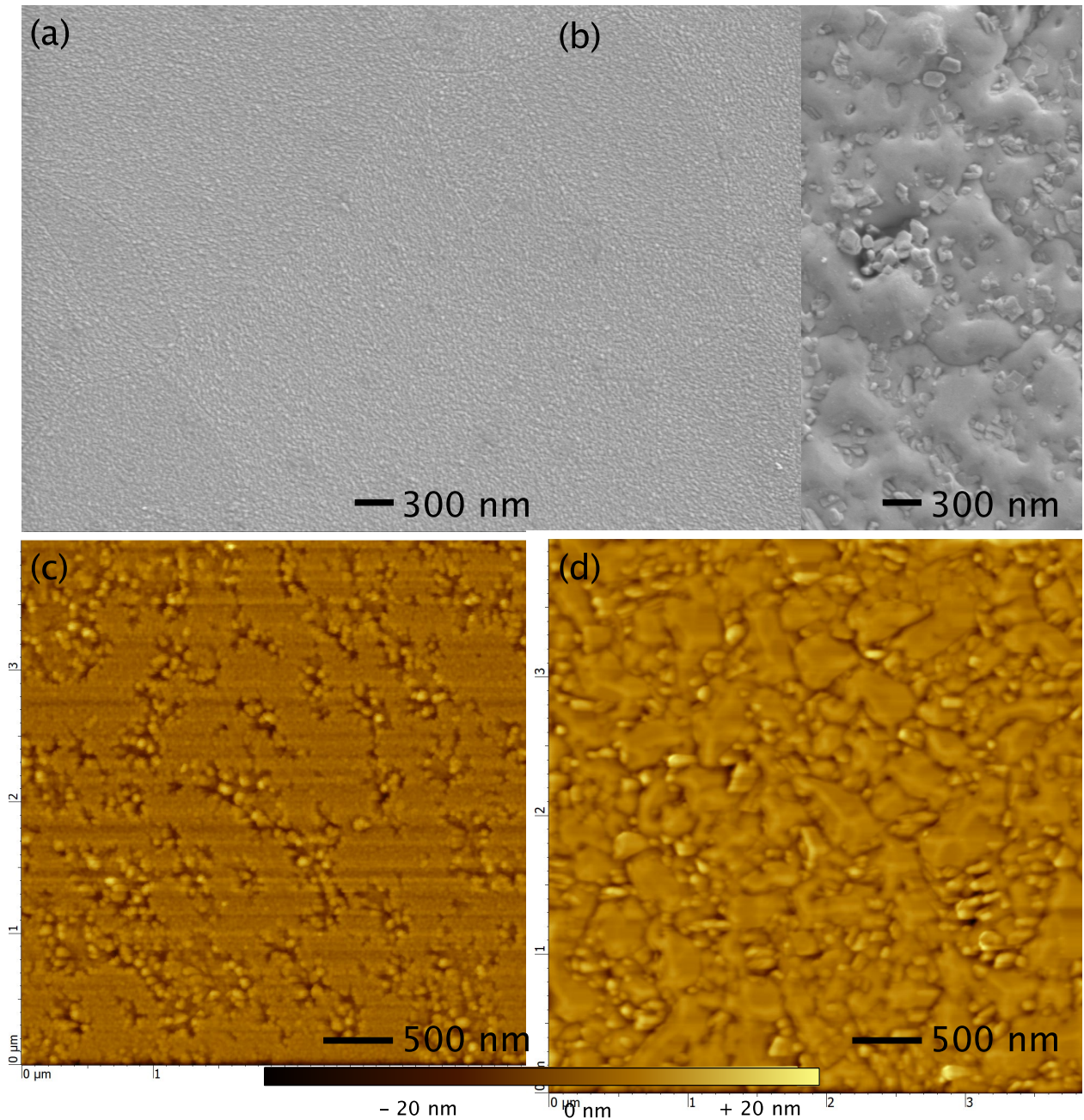

Figure 3. SEM micrographs: (a) TiO$_2$ sample; (b) BT750 sample; AFM micrographs of (c) TiO$_2$ sample; (d) BT750 sample.

The TEM micrograph (Figure 4a) of the BT750 sample's cross-section revealed a structure composed of interconnected grains with varying sizes (~50 to ~100 nm in diameter). EDX elemental mapping of the sample's cross-section revealed a heterogeneous distribution of the Bi and Ti elements, with distinct "bismuth rich" and "bismuth poor" areas (Figure 4b). This is in accordance with the $Bi_{12}TiO_{20}$ and $Bi_4Ti_3O_{12}$ phases identified by XRD analysis, which would correspond to the "bismuth rich" and "bismuth poor" areas, respectively. HRTEM micrographs were used verify the crystalline phase(s) of the material's matrix and the presence of angular crystallites, previously discovered via XRD and FEG-SEM analysis, respectively. The d-spacing was estimated at ~3.2 and ~3 Å for the matrix (Figure 4c) and the crystallite (Figure 4d), respectively. These interplanar distances correspond to the (013) plane of the $Bi_{12}TiO_{20}$ phase for the matrix and to the (711) plane of the $Bi_4Ti_3O_{12}$ phase for the crystallites. The presence of the above-mentioned phases is in agreement with the XRD results.
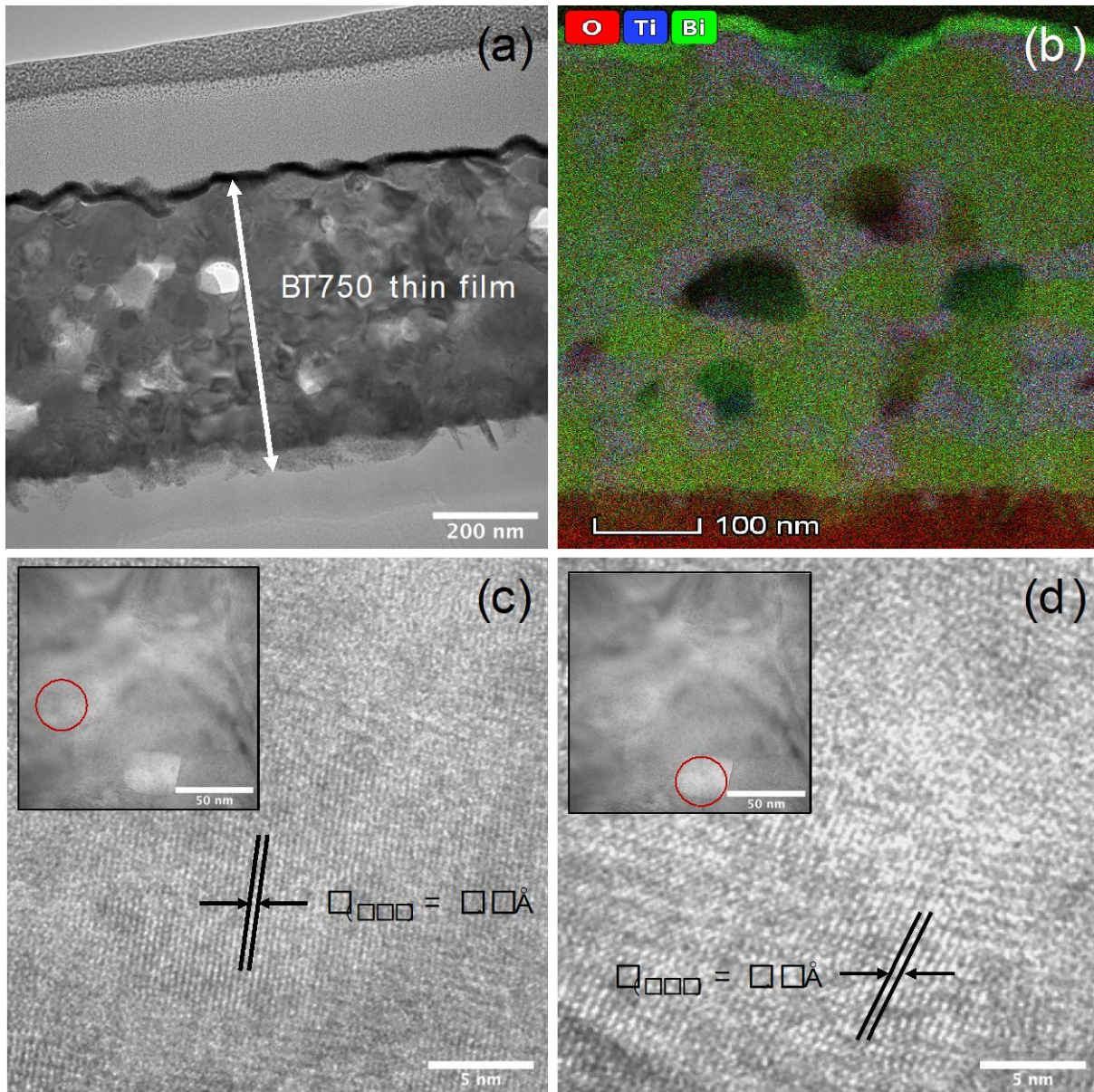
Figure 4. Cross-sectional TEM micrographs of the BT750 thin film deposited on soda-lime glass slides: (a) Morphology of coating at low magnification, (b) EDX elemental mapping , (c) HRTEM micrograph of the $Bi_{12}TiO_{20}$ (013) phase, (d) HRTEM micrographs of the $Bi_3Ti_4O_{12}$ (711) phase.

The optical band gap energy of the crystalline semiconductors was estimated using the Tauc plot method [34], by plotting $(\alpha h\nu)^{1/2}$ as a function of $h\nu$ and extrapolating the linear region to the abscissa (where α is the absorbance coefficient, h is Plank's constant, ν is the frequency of vibration). The BT750 and TiO_2 samples bandgap energy values were estimated at 2.82 and 3.2 eV, respectively (Figure 5). The bandgap of BT750 was significantly lower, compared to that of TiO_2, meaning it can

be photoactivated with a broader range of wavelengths. Our estimated value for titanium dioxide is in accordance with published data, as its bandgap is typically reported as 3.2 eV [35]. The same applies for BT750, as Fang *et al.* estimated the band gap values of $Bi_4Ti_3O_{12}$ and $Bi_{12}TiO_{20}$ at 3.03 and 2.59 eV, respectively [24]. Additionally, Du *et al.* studied a similar $Bi_{12}TiO_{20}/Bi_4Ti_3O_{12}$ composites produced by solid synthesis calcination and found band gap values ranging from 2.96 and 2.84 eV [21].
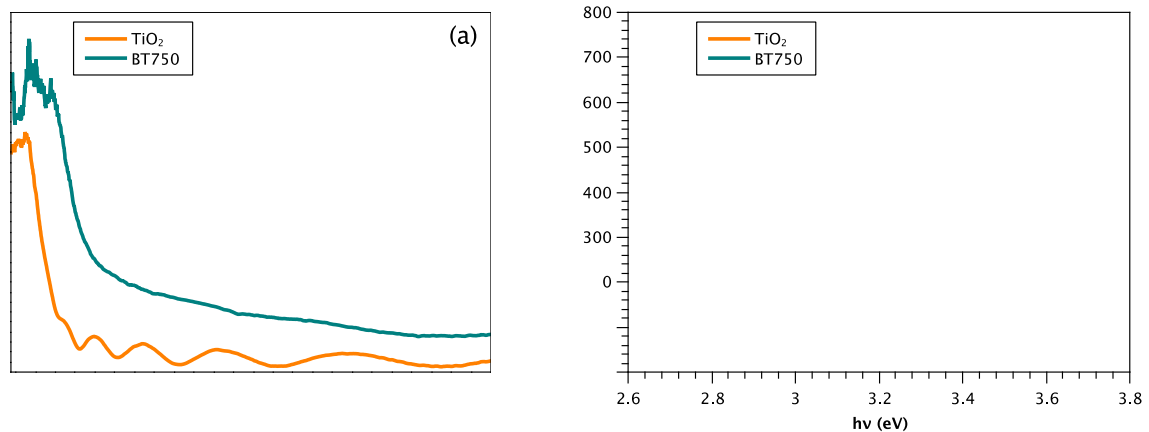

Figure 5. UV-Vis absorption spectra for TiO_2 and BT750 samples (a) and corresponding Tauc plots (b).

3.3. Photocatalytic characterisation of materials

The photocatalytic activity of the prepared TiO_2 and BT750 samples was initially assessed by monitoring the removal of methylene blue (MB) over time under UV-A light irradiation. The test was performed for uncoated glass (used as reference sample), BT750 and TiO_2 coatings. As shown in Figure 6a, adsorption-desorption equilibrium was reached after 1 hour in the dark, with no significant variation across all samples. Under UV-A irradiation no significant MB degradation was observed for the uncoated glass sample, while for both TiO_2 and BT750, the MB concentration gradually decreased under the irradiation. The photocatalytic performances of the two photocatalysts were compared by monitoring the main absorbance peak of MB under UV and over time. The pseudo-first order constant k was extracted using $Ln(A_0/A_t) = kt$, where A is the absorbance measured at 664 nm and t the time. Pseudo-first order constant k values of 0.18, 0.52

and 1.40 $(10^{-5}s^{-1})$ were obtained for uncoated glass, TiO$_2$ and BT750 samples, respectively. Although TiO$_2$ and BT750 coatings have a similar thickness and roughness, BT750 clearly outperformed TiO$_2$ with a photocatalytic activity 3 times higher.

Since stability and reusability of photocatalysts are of extreme importance for practical application, the reusability of the photocatalysts was assessed during 15 consecutive cycles of MB degradation tests under UV-A. Surprisingly, as shown in Figure 6c, there was a clear trend of increased photocatalytic activity for BT750 with each consecutive cycle. The bismuth titanate composite pseudo-first order constant k rose up to 7.76 $(10^{-5}s^{-1})$ after the 15th cycle, which translates to a 6-folds increase when compared to the 1st cycle. To put things into perspective, after its 15th cycle, BT750 was 15 times more efficient at degrading MB under UV than TiO$_2$. When the same test was performed for the TiO$_2$ sample, there were no noticeable changes in activity over 15 cycles of consecutive use. In both cases, repeated usage did not affect the surface roughness value (R$_a$) of the samples, therefore, the increased photocatalytic activity of bismuth titanate cannot be attributed to increased area of contact with pollutant in this case.

Following the dye degradation tests, the photocatalytic properties of bismuth titanate and titanium dioxide samples were compared, based on their ability to inactivate *Escherichia coli* (*E.coli* – the model microorganism was selected based on recommendations of ISO 27447 [31], also being a significant indicator of poor water quality) under UV-A irradiation. The results are presented in Figure 6d. The intensity of UV light was adjusted (by keeping the required distance between the light source and sample surface constant) to the level recommended in ISO 27447 standard of 0.25 mW cm^{-2} to rule out photoinactivation of the microorganism by means of UV light itself. Similar to the MB degradation tests, antimicrobial properties of BT750 samples were compared to those of TiO$_2$ coatings, while uncoated glass was used as reference; the tests were performed both under UV-A irradiation, and in the dark. As evident in Figure 6d, BT750 samples were able to reduce the number of viable *E. coli* cells in suspension to below the level of detection within 48 hours of UV-A

irradiation. When comparing irradiated vs non-irradiated samples, BT750 was the only material to demonstrate a statistically significant ($p < 0.05$) antimicrobial effect after 24 hours, with 1.61×10^6 CFU/mL fewer cells recovered when compared to its corresponding dark control. No other irradiated vs non-irradiated comparisons demonstrated a statistically significant antimicrobial effect. At the 48-hour mark, the number of cells recovered from the BT750 sample was nil, compared to the 2.9×10^5 CFU/mL recovered from the non-irradiated BT750 sample. The number of cells recovered from TiO_2 and uncoated glass, both irradiated and non-irradiated, as well as BT750 non-irradiated samples remained relatively consistent across the 48 hours. These results clearly highlight the more efficient photocatalytic activity of BT750 against both model pollutants and microorganisms when compared to the well-established TiO_2.
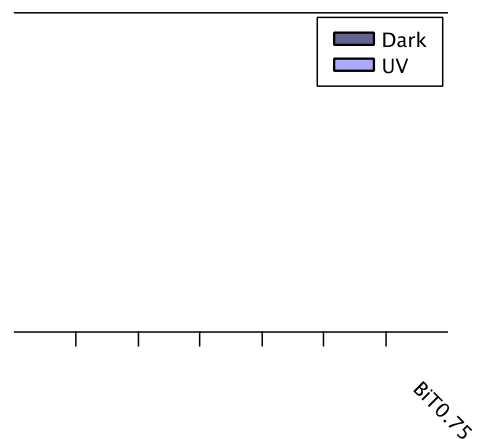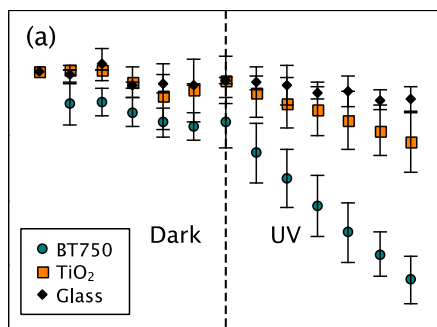

Figure 6. Photocatalytic activity assessment; (a) MB concentration in the dark and under UV when exposed to BT750, TiO₂ and uncoated glass; (b) Pseudo-first-order reaction rate plotted for MB removal, calculated for BT750, TiO₂ and uncoated glass under UV light; (c) MB pseudo-first-order reaction rate calculated for TiO₂ and BT750 over 15 consecutive cycles; (d) E. coli CFU/mL after 24, 48

hours on different materials and under different irradiation conditions, * represents statistically significant difference (p<0.05).

3.4. Analysis of the cycled sample

Along with a photocatalytic activity change, the colour of the coating changed from white to black at the end of the cycling experiment. Hence, the cycled sample was termed "BT750 – Black" to avoid confusion with the pristine sample which is termed BT750. XRD analysis at different grazing angles (from 0.3° to 5°) was performed to assess crystalline phases distribution through the bulk of the sample; it did not reveal significant difference between BT750 and BT750 – Black (Figure 7), which implies that there was no phase composition, crystal size nor orientation change after the cycling experiment (Figure 7). Additionally, the same 80:20 ratio of $Bi_{12}TiO_{20}$ to $Bi_4Ti_3O_{12}$ phases was estimated by direct derivation method at every grazing angles, suggesting a homogeneous phase distribution in the thin film (bulk and surface).
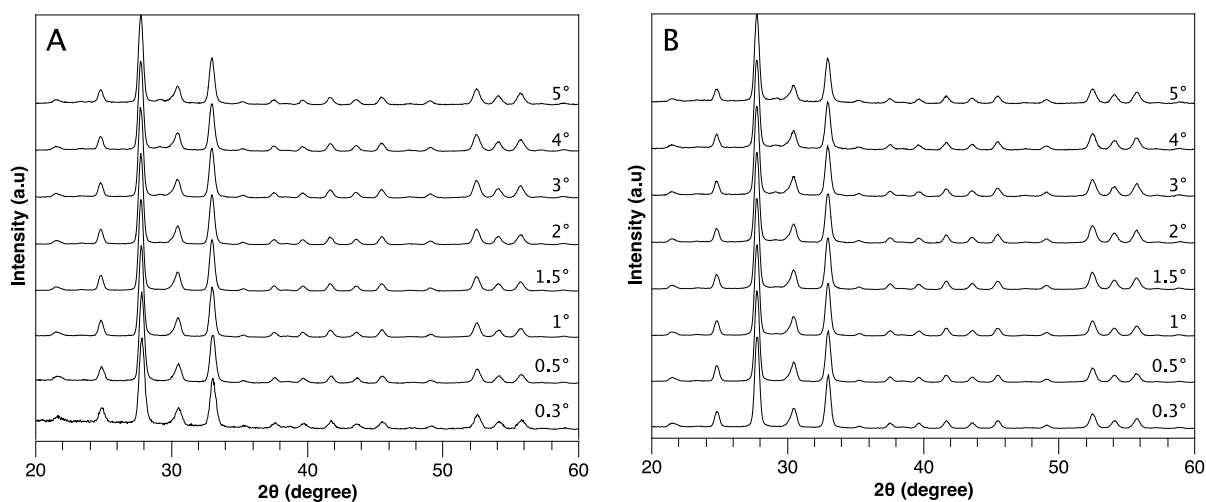

Figure 7. XRD analysis at different incident angle of (A) BT750 and (B) BT750 – Black.

Hence, to understand the origin of the increased photocatalytic activity observed during the reusability assessment, the chemical and electronic states of the BT750 and BT750 – Black coatings were investigated by XPS analysis. For reference, a pristine TiO_2 sample (TiO_2-a) was analysed and compared to one that was cycled (TiO_2-b). The results of the XPS analysis for TiO_2 and BT750 are

presented in Figure 8 and Figure 9, respectively. Gaussian functions were used for deconvolution of individual peaks. The carbon 1s peak was observed on survey spectra of all samples (not shown here) at 284.8 eV and attributed to adventitious carbon; the binding energies were referenced to this peak. High-resolution spectra of Ti 2p and O 1s peaks for the titanium dioxide coatings are presented in Figure 8 (a, b) for TiO_2-a and Figure 8 (c, d) for TiO_2-b, respectively. It is clear that the Ti 2p spectra of TiO_2-b (cycled) and TiO_2-a (pristine) samples had no significant variation; with two peaks attributed to Ti^{4+} $2p_{3/2}$ at 458.3 eV and Ti^{4+} $2p_{1/2}$ at 464.1 eV clearly visible in each case. From the absence of Ti^{3+} 2p peaks (typically observed at 457.1 eV and 462.9 eV [36], [37]), it can be concluded that for both of the TiO_2 samples Ti was found in the Ti^{4+} oxidation state. The O 1s peak for TiO_2-a sample (Figure 8b) can be deconvoluted into two peaks at 529.6 and 531.5 eV, that are typically attributed in literature to lattice oxygen (O 1s L) and oxygen vacancies or defects (O 1s V) [38]. The same two peaks can be seen on the high-resolution O 1s XPS spectrum in TiO_2-b sample (Figure 8d), however the presence of a third peak at 532.4 eV is evident, corresponding to chemisorbed oxygen species O 1s C [38]. The oxygen vacancy peak, O 1s V, is indicative of the presence of oxygen vacancies (O^-, O_2^-) in the lattice of the metal oxide, while the chemisorbed oxygen peak, O 1s C, is indicative of the presence of loose oxygen species on the surface of the sample, from H_2O or M-OH. Therefore, the presence of a third peak on the high-resolution O 1s XPS spectrum of the TiO_2-b sample is in good agreement with the fact that after 15 cycles in aqueous solution of MB dye there is a considerable amount of chemisorbed oxygen on the sample surface, compared to its unused counterpart. It is notable that for both TiO_2-a and TiO_2-b, the atomic percentage ratio of the lattice oxygen peak to oxygen vacancy peak was calculated (from relative areas of the peaks) as 2:1. The latter finding is in good agreement with MB degradation data, where the photocatalytic activity of the titanium dioxide sample, unlike BT750, remained stable over 15 consecutive testing cycles.
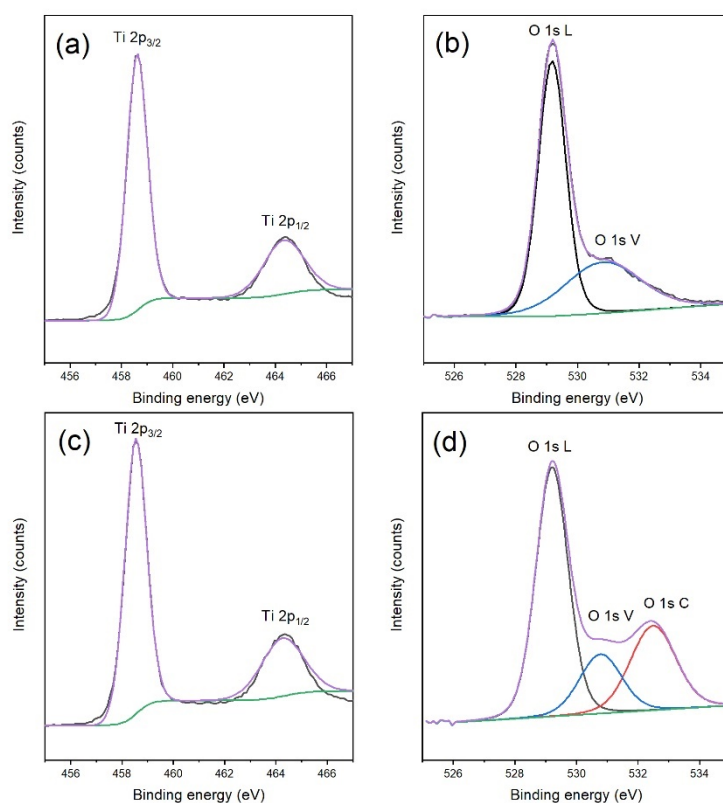
Figure 8. High-resolution XPS spectra of TiO₂-a (pristine) sample: (a) Ti 2p spectrum, (b) O 1s spectrum; and TiO₂-b (cycled) sample: (c) Ti 2p spectrum, (d) O 1s spectrum.

High-resolution XPS spectra of BT750 and BT750 – Black samples are shown in *Figure 9*. Thus, *Figure 9* (a) and (d) depict the Bi 4f peak for BT750 and BT750 – Black samples, respectively. Clearly, no significant differences in peaks shape can be observed in this case. The spectrum of BT750 reveals two peaks at 158.9 and 164.3 eV that can be assigned to the binding energies of Bi 4f7/2 and Bi 4f5/2 states, which is in good agreement with the literature information [39]. However, for the Bi 4f spectrum on the BT750 – Black sample, there is a shift of the peaks of ca. 0.8 eV towards lower binding energies. For bismuth oxide-based photocatalysts the latter is typically attributed to the presence of additional oxygen vacancies [40]. Absence of additional shoulder peaks next to the main peaks is believed to be indicative of the presence of only the Bi³⁺ oxidation state for both BT750 and BT750 – Black samples [41]. The Ti 2p spectrum (presented in *Figure 9* (b, e) for BT750 and BT750 -

Black, respectively) partially overlaps with Bi 4d, also in good agreement with the information found in the literature [42]. Deconvolution of the Ti 2p spectra in each case reveals three peaks, namely Ti^{4+} 2p3/2 at 458.3 eV and Ti^{4+} 2p1/2 at 464.1 eV, as well as Bi 4d3/2 at 466.1 eV. In this case, due to strong peak overlapping, it is difficult to estimate the likelihood of the presence of Ti^{3+} 2p peaks next to the Ti^{4+} 2p peaks, though as the Ti^{3+} 2p3/2 peak is typically observed at binding energy of 457.1 eV, it is rather likely that, similarly to TiO_2, in the BT750 sample Ti was in the Ti^{4+} oxidation state. O 1s high-resolution spectra are shown in *Figure 9* (c) and (f) for BT750 and BT750 - Black, respectively. Similarly, to the TiO_2 sample analysed earlier, O 1s peak of BT750 can be deconvoluted into two peaks, corresponding to lattice oxygen (O 1s L) and oxygen vacancies (O 1s V), while an additional peak attributed to chemisorbed oxygen can be clearly seen on the spectrum of BT750 - Black. However, in contrast to TiO_2 samples, the atomic percentage ratio of O 1s L to O 1s V (from relative areas of the peaks) changed from ca. 4:1 for the BT750 to ca. 0.7:1 for the BT750 - Black. The latter is clearly indicative of a significantly higher number of oxygen vacancies / defects being present in the BT750 – Black sample after cycling tests, and is good agreement with MB degradation test results, where a 6-fold increase in activity was observed after 15 cycles of use.
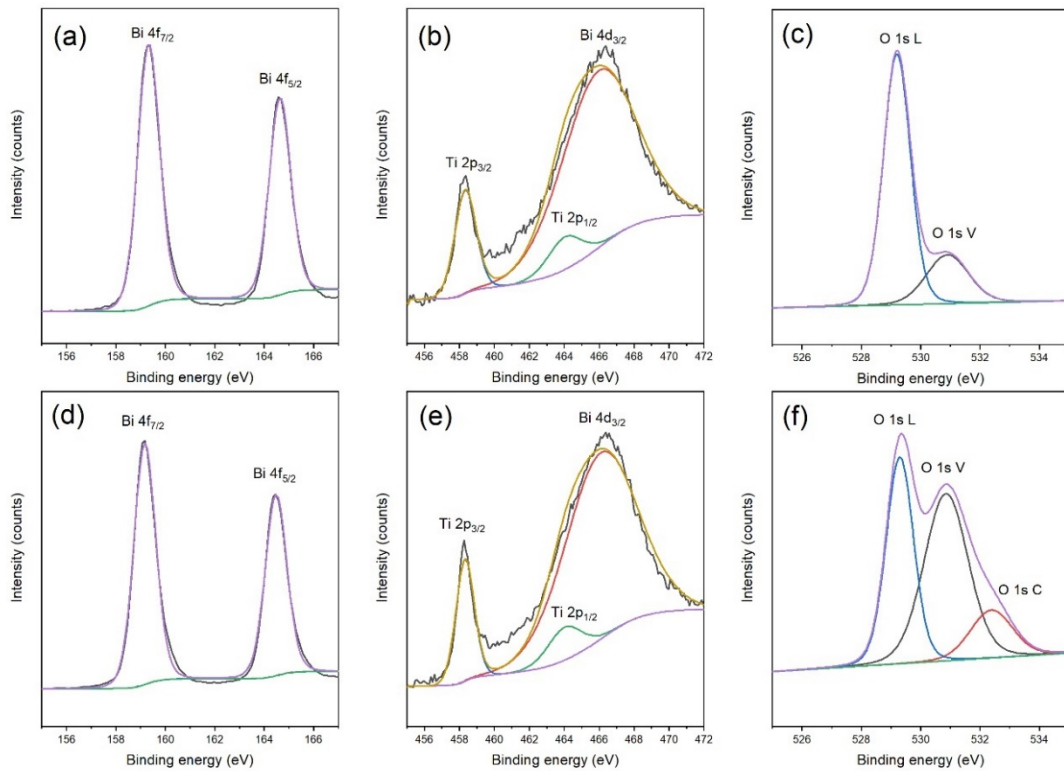
Figure 9. High-resolution XPS spectra of BT750 sample: (a) Bi 4f spectrum, (b) Bi 4d and Ti 2p spectrum, (c) O 1s spectrum; and BT750 – Black: (d) Bi 4f spectrum, (e) Bi 4d and Ti 2p, (f) O 1s spectrum.

For further insights into the increased photocatalytic activity of the $Bi_{12}TiO_{20}/Bi_4Ti_3O_{12}$ samples, time-resolved photoluminescence (TRPL) was used to evaluate the dynamics of photogenerated charge carriers of BT750, BT750 – Black and TiO_2 samples. As no variation in neither photocatalytic activity nor XPS results was observed after cycling, for the TiO_2 samples, the PL was only performed on an unused titanium dioxide coating. The PL decay graphs, as well as corresponding residuals are presented in Figure 10. All the decay curves obtained can be well described by simple multi-exponential decay model [43], [44] (Eq. (1)), where τ is the electron lifetime, β is the shape factor and A is a baseline correction factor. The average lifetime of the photogenerated species, τ_{avg} was estimated using (Eq. (2)).

$$\hat{Y} = A + \sum_{i}^{n} \beta_i \times e^{(-t/\tau_i)} \qquad (1)$$

$$\tau_{avg} = \frac{\sum_{i}^{n} \beta_i \times \tau_i^2}{\sum_{i}^{n} \beta_i \times \tau_i} \qquad (2)$$

The model accurately described the PL signal decay in all investigated samples, with χ^2 values close to 1 and residuals symmetrically distributed, clustering towards the middle of the plot (Figure 10 (b-d)). The parameters used to fit exponential decay curves are listed in Table 3. All the PL curves show charge carrier lifetimes in the microsecond range, while PL curves can be separated into three exponential decay components. The first component is related to the fast recombination of excitons, occuring around ~10 μs. While the two other components are related to slow recombinations of excitons, occuring around ~30 and ~90 μs, respectively. BT750 was fitted with only two components, which was attributed to its lower signal. Regardless, the photogenerated species' average lifetime was similar for both BT750 and TiO$_2$ at 40 ~μs, while BT750 – Black had an average lifetime of ~52 μs. This significant increase is mainly due to the longest lasting photogenerated species identified in BT750 – Black, with a τ_3 of ~112 μs, which is double the lifetime of titania's τ_3. The electron lifetime of the third exponential decay component is believed to favour the photocatalytic activity of semi-conductors, since it indicates an increased permanence of long living excited states [45]. Hence, these photogenerated species are the most likely to diffuse to the surface of a photocatalyst without recombining. Thus, it is evident from the PL data after cycling the bismuth titanate composite, photogenerated charge carriers had a longer lifetimes, that can be attributed to oxygen vacancy-mediated efficient charge separation and lower recombination rates of photogenerated electron-hole pairs [40], [45]. These results are in accordance with the MB degradation cycling tests, as prolonged lifetime of charge carries results in higher degradation rates of the model pollutant.
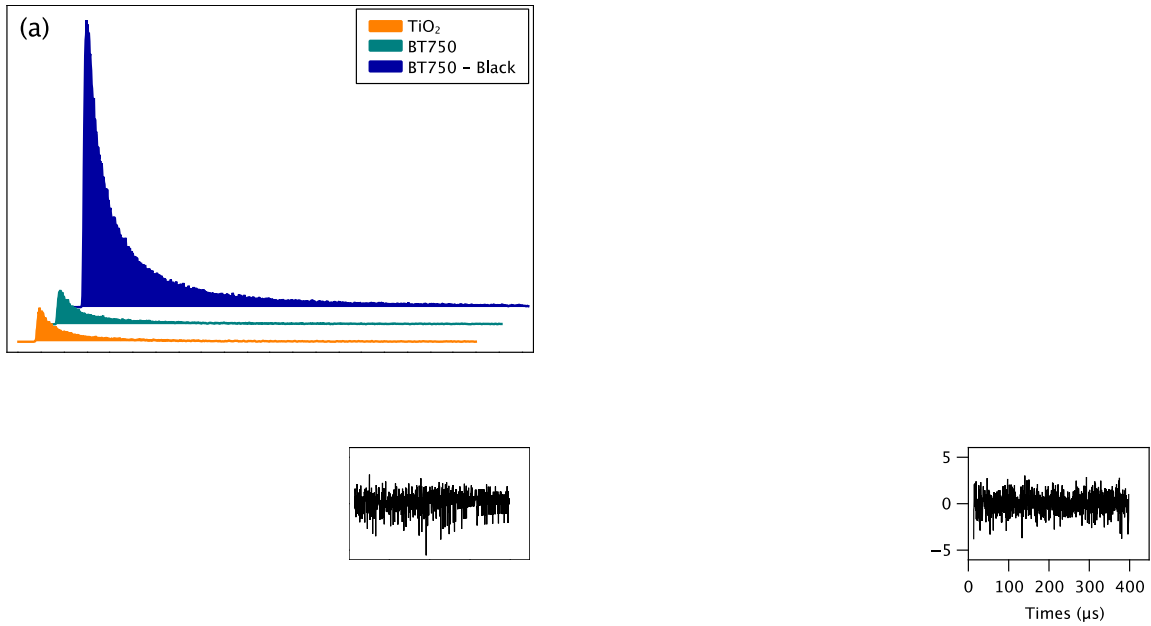
Figure 10. Time-resolved photoluminescence spectra for: (a) TiO_2, BT750, BT750 – Black; (b) TiO_2 with fitted model and residuals; (c) BT750 with fitted model and residuals; (c) BT750 – Black with fitted model and residuals.

Table 3. Curve-fitting results of the decay curves measured for BT750, BT750 - Black and TiO_2.

Sample	Peak excitation wavelength	β_1	τ_1	β_2	τ_2	β_3	τ_3	τ_{avg}	χ^2
	nm	-	(µs)	-	(µs)	-	(µs)	(µs)	-
TiO_2	510	148.0	7.0	123.0	22.2	48.0	66.6	40.3	0.99
BT750	540	222.2	11.6	8.3	56.8	-	-	40.8	1.09
BT750 – Black	540	1483.0	8.8	1153.0	30.3	239.8	112.1	52.2	1.06

3.5. Discussion

The synthesized bismuth titanate composite, $Bi_{12}TiO_{20}/Bi_4Ti_3O_{12}$, has displayed high photocatalytic activity under UV light and consistently outperformed TiO_2 in every test. Interestingly, after repeated use, the sample changed colour from white (BT750) to black (BT750 – Black) and its photocatalytic activity increased 6-folds. The XPS analysis of the samples has shown an O 1s L to O 1s V ratio change

from 4:1 to 0.7:1, for BT750 and BT750 – Black, respectively. This significant increase in the O 1s V

peak is believed to be linked to a higher concentration of oxygen vacancies in the thin film.

This type of behaviour has previously been reported by several authors, for bismuth-based

photocatalysts such as BiOCl [46]–[48]. Ye *et al.* prepared black BiOCl samples by exposing pristine

BiOCl powders to UV light [46], [47]. The photocatalytic activity and visible light absorption of the UV

treated BiOCl sample increased significantly compared to the pristine ones. UV-induced oxygen

vacancies were identified by XPS, EPR and PL analysis and found to be responsible for the 20-fold

increase in photocatalytic activity under visible light. Oxygen vacancies form mid gap states below

the conduction band, acting as electron trapping sites, improving the electron-hole separation, and

thus the photocatalytic activity [46].

This is consistent with the results of our TRPL analysis, as charger carriers photogenerated by BT750

– Black had a significantly longer lifetime than the one photogenerated by BT750. The oxygen

vacancies identified by XPS in BT750 – Black, may act as electron traps, increasing the lifetime of

charge carriers and improving the photocatalytic activity, as shown during the cycling tests. The

mechanism behind UV induced oxygen vacancy formation is still unclear, but *Ye et al.* attributed it to

the low bond energy and long bond length of the Bi–O bond [47].

Conclusion

In the present study, bismuth titanate photocatalytic coatings were successfully synthesised by

means of pDC reactive magnetron co-sputtering, reportedly for the first time. Variation of power

applied to the titanium target, as well as investigation of optimum annealing temperature and

length of thermal treatment, allowed the synthesis of highly active $Bi_{12}TiO_{20}$ / $Bi_4Ti_3O_{12}$ composite,

significantly outperforming conventionally used titanium dioxide under UV-A irradiation in both dye

degradation and bacterial inactivation tests. Thus, being characterised with comparable thickness

and surface roughness values, bismuth titanate was found to be 3 times more efficient in MB

degradation tests, as well as reducing the number of viable *E. coli* cells in suspension to below the

limit of detection after 48 h of irradiation. Furthermore, unlike titanium dioxide, bismuth titanate

was shown to be capable of developing additional oxygen vacancies over multiple use cycles,

resulting in formation of longer-living photogenerated charge carriers and enhanced photocatalytic

activity. Thus, in reusability assessments over 15 consecutive cycles of use, the photocatalytic

activity of bismuth titanate increased 6-fold compared to the first use of the sample. Owing to the

simplicity and excellent scalability of the deposition technique used, as well as the high

photocatalytic efficiency of the studied material, we believe the findings of the present study are of

high relevance to those working on enhancement of photocatalytic activity for water treatment

applications, both in the laboratory and industrial environments.

Acknowledgements

References

[1]   'Drinking-water', *World Health Organization*, 2019. https://www.who.int/news-room/fact-sheets/detail/drinking-water (accessed Jan. 13, 2020).

[2]   A. K. Gain, C. Giupponi, and Y. Wada, 'Measuring global water security towards sustainable development goals', *Environ. Res. Lett.*, vol. 11, no. 12, p. 124015, Dec. 2016, doi: 10.1088/1748-9326/11/12/124015.

[3]   C. Byrne, G. Subramanian, and S. C. Pillai, 'Recent advances in photocatalysis for environmental applications', *Journal of Environmental Chemical Engineering*, vol. 6, no. 3, pp. 3531–3555, Jun. 2018, doi: https://doi.org/10.1016/j.jece.2017.07.080.

[4]   M. Ratova, J. Redfern, J. Verran, and P. J. Kelly, 'Highly efficient photocatalytic bismuth oxide coatings and their antimicrobial properties under visible light irradiation', *Applied Catalysis B: Environmental*, vol. 239, pp. 223–232, Dec. 2018, doi: 10.1016/j.apcatb.2018.08.020.

[5]   J. Redfern and M. C. Enright, 'Further understanding of Pseudomonas aeruginosa's ability to horizontally acquire virulence: possible intervention strategies', *Expert Review of Anti-infective Therapy*, vol. 0, no. ja, p. null, Apr. 2020, doi: 10.1080/14787210.2020.1751610.

[6]   A. Fujishima and K. Honda, 'Electrochemical photolysis of water at a semiconductor electrode', *Nature*, vol. 238, no. 5358, pp. 37–38, Jul. 1972.

[7]   A. Fujishima, X. Zhang, and D. A. Tryk, 'TiO2 photocatalysis and related surface phenomena', *Surface Science Reports*, vol. 63, no. 12, pp. 515–582, Dec. 2008, doi: 10.1016/j.surfrep.2008.10.001.

[8] X. Chen, L. Liu, and F. Huang, 'Black titanium dioxide (TiO2) nanomaterials', *Chem. Soc. Rev.*, vol. 44, no. 7, pp. 1861–1885, Mar. 2015, doi: 10.1039/C4CS00330F.

[9] S. A. Ansari, M. M. Khan, M. O. Ansari, and M. H. Cho, 'Nitrogen-doped titanium dioxide (N-doped TiO2) for visible light photocatalysis', *New J. Chem.*, vol. 40, no. 4, pp. 3000–3009, Apr. 2016, doi: 10.1039/C5NJ03478G.

[10] I. Suhariadi, M. Shiratani, and N. Itagaki, 'Morphology Evolution Of ZnO Thin Films Deposited By Nitrogen Mediated Crystallization Method', *MATEC Web of Conferences*, vol. 159, p. 02008, Jan. 2018, doi: 10.1051/matecconf/201815902008.

[11] Z. Shi *et al.*, 'TiO2/MoS2 heterojunctions-decorated carbon fibers with broad-spectrum response as weaveable photocatalyst/photoelectrode', *Materials Research Bulletin*, vol. 112, pp. 354–362, Apr. 2019, doi: 10.1016/j.materresbull.2019.01.005.

[12] J. C. Medina, N. S. Portillo-Vélez, M. Bizarro, A. Hernández-Gordillo, and S. E. Rodil, 'Synergistic effect of supported ZnO/Bi2O3 heterojunctions for photocatalysis under visible light', *Dyes and Pigments*, vol. 153, pp. 106–116, Jun. 2018, doi: 10.1016/j.dyepig.2018.02.006.

[13] K. K. Bera, R. Majumdar, M. Chakraborty, and S. K. Bhattacharya, 'Phase control synthesis of α, β and α/β Bi2O3 hetero-junction with enhanced and synergistic photocatalytic activity on degradation of toxic dye, Rhodamine-B under natural sunlight', *Journal of Hazardous Materials*, vol. 352, pp. 182–191, Jun. 2018, doi: 10.1016/j.jhazmat.2018.03.029.

[14] W. Zhao *et al.*, 'A novel Z-scheme Ag3VO4/BiVO4 heterojunction photocatalyst: Study on the excellent photocatalytic performance and photocatalytic mechanism', *Applied Catalysis B: Environmental*, vol. 245, pp. 448–458, May 2019, doi: 10.1016/j.apcatb.2019.01.001.

[15] L. Zhang, W. Wang, L. Zhou, and H. Xu, 'Bi2WO6 Nano- and Microstructures: Shape Control and Associated Visible-Light-Driven Photocatalytic Activities', *Small*, vol. 3, no. 9, pp. 1618–1625, 2007, doi: 10.1002/smll.200700043.

[16] W. F. Yao *et al.*, 'Photocatalytic property of perovskite bismuth titanate', *Applied Catalysis B: Environmental*, vol. 52, no. 2, pp. 109–116, Sep. 2004, doi: 10.1016/j.apcatb.2004.04.002.

[17] W. Feng Yao *et al.*, 'Photocatalytic property of bismuth titanate Bi12TiO20 crystals', *Applied Catalysis A: General*, vol. 243, no. 1, pp. 185–190, Mar. 2003, doi: 10.1016/S0926-860X(02)00564-1.

[18] L. Wang *et al.*, 'Bi4Ti3O12 Synthesized by High Temperature Solid Phase Method and it's Visible Catalytic Activity', *Procedia Environmental Sciences*, vol. 18, no. Supplement C, pp. 547–558, Jan. 2013, doi: 10.1016/j.proenv.2013.04.074.

[19] M. Valant and D. Suvorov, 'Processing and Dielectric Properties of Sillenite Compounds Bi12MO20−δ (M = Si, Ge, Ti, Pb, Mn, B1/2P1/2)', *Journal of the American Ceramic Society*, vol. 84, no. 12, pp. 2900–2904, Dec. 2001, doi: 10.1111/j.1151-2916.2001.tb01112.x.

[20] T. Kikuchi, A. Watanabe, and K. Uchida, 'A family of mixed-layer type bismuth compounds', *Materials Research Bulletin*, vol. 12, no. 3, pp. 299–304, Mar. 1977, doi: 10.1016/0025-5408(77)90148-9.

[21] C. Du *et al.*, 'Design and simple synthesis of composite Bi12TiO20/Bi4Ti3O12 with a good photocatalytic quantum efficiency and high production of photo-generated hydroxyl radicals', *Phys. Chem. Chem. Phys.*, vol. 18, no. 38, pp. 26530–26538, Sep. 2016, doi: 10.1039/C6CP05223A.

[22] A. Meng, J. Xing, W. Guo, Z. Li, and X. Wang, 'Electrospinning synthesis of porous Bi12TiO20/Bi4Ti3O12 composite nanofibers and their photocatalytic property under simulated sunlight', *J Mater Sci*, vol. 53, no. 20, pp. 14328–14336, Oct. 2018, doi: 10.1007/s10853-018-2628-2.

[23] S. Khodadoost, A. Hadi, J. Karimi-Sabet, M. Mehdipourghazi, and A. Golzary, 'Optimization of hydrothermal synthesis of Bismuth titanate nanoparticles and application for photocatalytic degradation of Tetracycline', *Journal of Environmental Chemical Engineering*, vol. 5, no. 6, pp. 5369–5380, Dec. 2017, doi: 10.1016/j.jece.2017.10.006.

[24] G. Fang, L. Wang, G. Zhang, X. Yan, and D. Wang, 'Rapid microwave-assisted sol-gel synthesis and exceptional visible light photocatalytic activities of Bi12TiO20', *Ceramics International*, vol. 44, no. 14, pp. 16388–16393, Oct. 2018, doi: 10.1016/j.ceramint.2018.06.048.

[25] P. J. Kelly and R. D. Arnell, 'Magnetron sputtering: a review of recent developments and applications', *Vacuum*, vol. 56, no. 3, pp. 159–172, Mar. 2000, doi: 10.1016/S0042-207X(99)00189-X.

[26] M. Yıldırım, 'Current conduction and steady-state photoconductivity in photodiodes with bismuth titanate interlayer', *Thin Solid Films*, vol. 615, pp. 300–304, Sep. 2016, doi: 10.1016/j.tsf.2016.07.040.

[27] G. Orozco-Hernández, J. J. Olaya, J. E. Alfonso, C. A. Pineda-Vargas, and C. Mtshali, 'Optical response of bismuth based thin films synthesized via unbalanced magnetron DC sputtering technique', *Thin Solid Films*, vol. 628, pp. 170–175, Apr. 2017, doi: 10.1016/j.tsf.2017.03.018.

[28] S. K. Badge and A. V. Deshpande, 'La3+ modified bismuth titanate (BLT) prepared by sol – gel synthesis: Structural, dielectric, impedance and ferroelectric studies', *Solid State Ionics*, vol. 347, p. 115270, Apr. 2020, doi: 10.1016/j.ssi.2020.115270.

[29] M. Grao, C. Amorim, R. Brito Portela Marcelino, and P. Kelly, 'Crystalline TiO2 supported on stainless steel mesh deposited in a one step process via pulsed DC magnetron sputtering for wastewater treatment applications', *Journal of Materials Research and Technology*, vol. 9, no. 3, pp. 5761–5773, May 2020, doi: https://doi.org/10.1016/j.jmrt.2020.03.101.

[30] M. Ratova, R. Klaysri, P. Praserthdam, and P. J. Kelly, 'Pulsed DC magnetron sputtering deposition of crystalline photocatalytic titania coatings at elevated process pressures', *Materials Science in Semiconductor Processing*, vol. 71, pp. 188–196, Nov. 2017, doi: 10.1016/j.mssp.2017.07.028.

[31] 'ISO 27447:2019(en), Fine ceramics (advanced ceramics, advanced technical ceramics) — Test method for antibacterial activity of semiconducting photocatalytic materials'. .

[32] B. Mihailova, G. Bogachev, V. Marinova, and L. Konstantinov, 'Raman spectroscopy study of sillenites. II. Effect of doping on Raman spectra of Bi12TiO20', *Journal of Physics and Chemistry of Solids*, vol. 60, no. 11, pp. 1829–1834, Nov. 1999, doi: 10.1016/S0022-3697(99)00195-X.

[33] M. Hasanuzzaman, A. Rafferty, M. Sajjia, and A.-G. Olabi, 'Properties of Glass Materials', in *Reference Module in Materials Science and Materials Engineering*, Elsevier, 2016.

[34] J. Tauc, 'Optical properties and electronic structure of amorphous Ge and Si', *Materials Research Bulletin*, vol. 3, no. 1, pp. 37–46, Jan. 1968, doi: 10.1016/0025-5408(68)90023-8.

[35] K. Madhusudan Reddy, S. V. Manorama, and A. Ramachandra Reddy, 'Bandgap studies on anatase titanium dioxide nanoparticles', *Materials Chemistry and Physics*, vol. 78, no. 1, pp. 239–245, Feb. 2003, doi: 10.1016/S0254-0584(02)00343-7.

[36] R. Klaysri, M. Ratova, P. Praserthdam, and P. J. Kelly, 'Deposition of Visible Light-Active C-Doped Titania Films via Magnetron Sputtering Using CO2 as a Source of Carbon', *Nanomaterials (Basel)*, vol. 7, no. 5, May 2017, doi: 10.3390/nano7050113.

[37] B. Bharti, S. Kumar, H.-N. Lee, and R. Kumar, 'Formation of oxygen vacancies and Ti^{3+} state in TiO_2 thin film and enhanced optical properties by air plasma treatment', *Scientific Reports*, vol. 6, p. 32355, Aug. 2016, doi: 10.1038/srep32355.

[38] A. Ghobadi, T. G. Ulusoy, R. Garifullin, M. O. Guler, and A. K. Okyay, 'A Heterojunction Design of Single Layer Hole Tunneling ZnO Passivation Wrapping around TiO 2 Nanowires for Superior Photocatalytic Performance', *Scientific Reports*, vol. 6, no. 1, Art. no. 1, Jul. 2016, doi: 10.1038/srep30587.

[39] M. Ratova, L. Tosheva, P. J. Kelly, and B. Ohtani, 'Characterisation and properties of visible light-active bismuth oxide-titania composite photocatalysts', *Sustainable Materials and Technologies*, vol. 22, p. e00112, Dec. 2019, doi: 10.1016/j.susmat.2019.e00112.

[40] M. Ji *et al.*, 'Oxygen vacancies modulated Bi-rich bismuth oxyiodide microspheres with tunable valence band position to boost the photocatalytic activity', *Journal of Colloid and Interface Science*, vol. 533, pp. 612–620, Jan. 2019, doi: 10.1016/j.jcis.2018.08.097.

[41] M. Lv *et al.*, 'Bismuth and chromium co-doped strontium titanates and their photocatalytic properties under visible light irradiation', *Phys. Chem. Chem. Phys.*, vol. 17, no. 39, pp. 26320–26329, Sep. 2015, doi: 10.1039/C5CP03889H.

[42] J. E. Alfonso, J. J. Olaya, M. J. Pinzón, and J. F. Marco, 'Potentiodynamic Polarization Studies and Surface Chemical Composition of Bismuth Titanate (BixTiyOz) Films Produced through Radiofrequency Magnetron Sputtering', *Materials (Basel)*, vol. 6, no. 10, pp. 4441–4449, Oct. 2013, doi: 10.3390/ma6104441.

[43] K. Fujihara, S. Izumi, T. Ohno, and M. Matsumura, 'Time-resolved photoluminescence of particulate TiO2 photocatalysts suspended in aqueous solutions', *Journal of Photochemistry and Photobiology A: Chemistry*, vol. 132, no. 1, pp. 99–104, Mar. 2000, doi: 10.1016/S1010-6030(00)00204-5.

[44] K. Wakabayashi, Y. Yamaguchi, T. Sekiya, and S. Kurita, 'Time-resolved luminescence spectra in colorless anatase TiO2 single crystal', *Journal of Luminescence*, vol. 112, no. 1, pp. 50–53, Apr. 2005, doi: 10.1016/j.jlumin.2004.09.080.

[45] M. V. Dozzi, C. D'Andrea, B. Ohtani, G. Valentini, and E. Selli, 'Fluorine-Doped TiO2 Materials: Photocatalytic Activity vs Time-Resolved Photoluminescence', *J. Phys. Chem. C*, vol. 117, no. 48, pp. 25586–25595, Dec. 2013, doi: 10.1021/jp4095563.

[46] L. Ye, K. Deng, F. Xu, L. Tian, T. Peng, and L. Zan, 'Increasing visible-light absorption for photocatalysis with black BiOCl', *Phys. Chem. Chem. Phys.*, vol. 14, no. 1, pp. 82–85, Dec. 2011, doi: 10.1039/C1CP22876E.

[47] L. Ye, L. Zan, L. Tian, T. Peng, and J. Zhang, 'The {001} facets-dependent high photoactivity of BiOCl nanosheets', *Chem. Commun.*, vol. 47, no. 24, pp. 6951–6953, Jun. 2011, doi: 10.1039/C1CC11015B.

[48] L. Zhang, W. Wang, D. Jiang, E. Gao, and S. Sun, 'Photoreduction of CO2 on BiOCl nanoplates with the assistance of photoinduced oxygen vacancies', *Nano Res.*, vol. 8, no. 3, pp. 821–831, Mar. 2015, doi: 10.1007/s12274-014-0564-2.